Tunnelling and Underground Space Technology 155 (2025) 106157

Contents lists available at ScienceDirect

Tunnelling and Underground Space Technology incorporating Trenchless Technology Research

journal homepage: www.elsevier.com/locate/tust

Exploring the axial performance of protective sheathed rock bolts through large-scale testing

Hadi Nourizadeh [a,b,*], Ali Mirzaghorbanali [a,b], Kevin McDougall [c], Naj Aziz [d]

[a] Centre for Future Materials (CFM), University of Southern Queensland, Toowoomba, QLD 4350, Australia
[b] School of Engineering, University of Southern Queensland, Springfield Central, QLD 4300, Australia
[c] School of Surveying and Built Environment, University of Southern Queensland, Toowoomba, QLD 4350, Australia
[d] School of Civil, Mining & Environmental Engineering, University of Wollongong, Wollongong, NSW 2500, Australia

ARTICLE INFO

Keywords:
Rock bolts
Protective sheath
Corrosive environment
Axial performance

ABSTRACT

Understanding the axial load transfer mechanism of rock bolts under diverse conditions is essential for optimizing reinforcement in rock structures, advancing our comprehension of rock support, and facilitating the design of robust engineering solutions. This paper reports the outcomes of an extensive experimental investigation, focusing on the axial behavior of protective sheathed rock bolts employed in corrosive environments, assessed through pullout tests. Three distinct testing setups were designed to evaluate comprehensively the performance of these rock bolts in various scenarios. The results indicated that the failure characteristics and axial behaviors of sheathed rock bolts differ significantly from conventional counterparts. The findings revealed two primary failure modes in sheathed rock bolts: bolt rupture and slip at the grout-sheath interface, based on the testing arrangement and encapsulation length. The lack of adhesion and interlocking at the grout-sheath interface prevents shear stress at the bolt-grout interface from reaching its maximum potential strength, resulting in grout damage manifesting as circumferential cracks. This, in turn, initiates crack formation, reducing the system's bond strength. Additionally, it causes slip at the grout-sheath interface to occur at lower pullout loads. It can be inferred that the inner surface of the plastic sheath lacks the necessary structural integrity to withstand high loads, significantly impacting bond stress distribution and failure modes. The results demonstrate that the protective sheath remains intact up to an axial displacement of 28 mm, irrespective of the testing configuration. Additionally, it was observed that the maximum bond stress at the bolt-grout interface falls within the range of 6–8.7 MPa, which is below the shear strength of the grout. Consequently, achieving failure at the bolt-grout interface is not feasible.

1. Introduction

Rock reinforcement is a widely utilized technique within the mining and construction industries, particularly in tunnels and underground excavations (Li, 2017; Nourizadeh et al., 2023b; Singh et al., 2020). The primary goal of this method is to enhance the stability and bolster the load-bearing capacity of the rock mass (Martín et al., 2011; Rastegarmanesh et al., 2022). Ensuring the integrity of the reinforcement is a key priority within these industries, as the failure of these materials can lead to substantial financial implications and pose a risk to human safety. In Australia, the predominant practice following rock excavation is to install a rock bolting system to provide primary support (Chen et al., 2022). This method known as the one of the most effective and economical ground support techniques comprises a wide range of materials and techniques (Grasselli, 2005; Singh et al., 2022). Rock bolts can be classified according to various criteria, including their anchoring mechanism, materials, application, installation, and the mode of reinforcement system (Li et al., 2014; Nourizadeh et al., 2023a; Thompson et al., 2012; Windsor, 1997). Regarding the mode of reinforcement system, rock bolts can be categorized as being either active or passive reinforcements (Fahimifar and Ranjbarnia, 2009; He et al., 2015; Li, 2017; Thompson et al., 2012). The core disparity between these methodologies resides in the fact that active rock bolts exert a force onto the rock immediately upon installation, while passive rock bolts hinge on the rock's internal movement to trigger the reinforcement procedure (Peter et al., 2022).

* Corresponding author at: Centre for Future Materials (CFM), University of Southern Queensland, Toowoomba, QLD 4350, Australia.
E-mail address: hadi.nourizadeh@unisq.edu.au (H. Nourizadeh).

https://doi.org/10.1016/j.tust.2024.106157
Received 1 December 2023; Received in revised form 8 March 2024; Accepted 20 October 2024
Available online 23 October 2024

Active rock bolts typically comprise plain steel rods equipped with a mechanical anchor (expansion shell) at one end, and a plate and nut on the other (Thompson et al., 2012; Windsor, 1997). These bolts are consistently tensioned post-installation. In situations requiring short-term use, the bolts are typically retained without grouting (Kilic et al., 2003). However, in cases necessitating long-life application, the resin or cementitious grout fills the space between the bolt and rock (Windsor, 1997). By contrast, for passive rock bolts, comprising fully grouted rock bolts and consistently frictional rock bolts like Swellex and Split Set, pre-tensioning is not feasible. Instead, the reinforcement element comes into play when the rock mass commences movement (Li et al., 2014).

Irrespective of the reasons for using rock bolts, they are usually manufactured from carbon steel, making them susceptible to corrosion due to the potential exposure to groundwater in their operational environments (Cao et al., 2013; Ma et al., 2013). Various forms of corrosion occur in rock bolts, including crevice, pitting, stress corrosion cracking (SCC), and organic corrosion (Chen et al., 2021; Wu et al., 2019). Among these, pitting stands out as the most challenging, as it reduces the cross-sectional area of the bar (Aziz et al., 2014). Corrosion can potentially undermine the load-bearing capacity of rock bolts through various mechanisms (Craig et al., 2021). These mechanisms include diminishing the strength characteristics of the bar due to cross-sectional area reduction, creating cracks on the rebar, and progressively weakening the adhesive bond with the surrounding material over time. A contemporary approach in tunnel design involves the utilization of rock bolts for enduring reinforcement. In the Australian context, it has become customary to designate a design lifespan of 50 to 100 years for these foundational support components. The life expectancy of rock bolts can be addressed by developing and applying corrosion protection measures that provide a substantial level of safety. Corrosion protection of rock bolts commonly relies on the coating of the steel bar including cathodic sacrificial coating (zinc, zinc chrome, zinc epoxy, etc.) and barrier-type coating (epoxy, polyurethane, plastic, etc.) (Ma et al., 2018). An additional solution to address the corrosion issue is using rock bolts with protective sheathing. The protective sheathed bolts introduce an innovative solution to rectify the shortcomings inherent in conventional reinforcement systems, particularly those stemming from corrosion vulnerabilities. Comprising a steel bar integrated with point anchor expansion shells and accompanying face plates, the protective sheathed bolts employ a hemispherical dome and a nut to establish tension against the rock at the exposed end of the bolt. Furthermore, the incorporation of grouting subsequent to the initial bolt installation contributes to the long-term reinforcement of the structure (Fig. 1). This bolt is placed within a corrugated high-density polyethylene (HDPE) sheath, designed to facilitate the grouting process once the bolt is in position. The hollow hemispherical dome component serves as the entry point for grout injection, through a designated hole within the dome.

Generally, the failure patterns of a bolting system define the ultimate load capacity of a rock bolt. Therefore, understanding the nature of any failure occurring in any reinforcement system is essential. Investigating failure behavior requires a deep understanding of load transfer mechanisms. Rock bolts can experience diverse loading scenarios, ranging from pure shear to tensile loading, often combined with, or compounded by, rotational forces. Nonetheless, when it comes to rock bolts embedded in tunnels, their common failure mode tends to be caused by tension.

The existing literature highlights the extensive number of laboratory tests undertaken to study the behavior of various rock bolt types, spanning both mechanically-anchored and frictionally-anchored variations. Nevertheless, despite these endeavors, a gap in research persists, particularly in the comprehensive examination of plastic sheathed rock bolts behavior where a combination of anchoring techniques is complemented by the inclusion of a protective sheath. One of the challenges linked to the inclusion of a protective plastic sleeve around the reinforcing tendon lies in guaranteeing the efficient transfer of loads among the tendon, the grout annuli, and the surrounding ground.

Despite prior studies on the performance of protective sheathed bolts specifically by Aziz et al. (2017), Bertuzzi (2004), and Villaescusa and Wright (1999), there is still a gap in comprehending the behavior of grouted sheathed rock bolts. This gap includes understanding the impact of encapsulation length on the axial performance of sheathed rock bolts, analyzing the distribution of bond stress along the encapsulation length compared to conventional rock bolts, and exploring the failure mode of the system under various loading and anchoring conditions. Aziz et al., (2017) conducted a laboratory investigation to assess the integrity of plastic-sheathed cable bolts in shear conditions. The outcomes of both single and double shear tests revealed that the corrugated plastic sheath exhibited noteworthy resistance against shear loads, enduring without substantial damage up to a maximum displacement of 33 mm. Villaescusa and Wright, (1999) conducted a series of laboratory and field experiments aimed at establishing the pullout strength of the components of sheathed bolts. This study focused on bolt rupture due to a relatively long encapsulation length in laboratory settings, and their in-situ testing considered the effects of host rocks, grouting, and ungrouting. Bertuzzi, (2004) conducted an assessment of corrosion-protective anchors situated within tunnels in Sydney, Australia. The study's outcome highlighted that the protective plastic sheaths sustained damage at an approximate shear movement of 15 mm.

This study addresses the existing gap through an extensive experimental investigation on a large scale. Our primary objective is to explore the axial load transfer mechanism of plastic-sheathed rock bolts across various scenarios, including different loading conditions and encapsulation lengths. Additionally, we examine the failure modes of the systems, aiming to identify the weakest components under pullout loading conditions in different scenarios. Furthermore, our innovative approach involves instrumenting the bolt along the encapsulation length, providing outstanding results that enhance our understanding of the bond behavior of this specific bolt type, an aspect previously overlooked. The outcomes of this study offer valuable insights into the behavior and performance of protective sheathed bolting systems under varying conditions, contributing to a deeper understanding of their mechanical response and potential vulnerabilities.

1.1. Experimental design

To comprehensively assess the axial behavior of corrosion protective sheathed bolts, three distinct experimental campaigns were implemented within the pullout testing program, as schematically depicted in Fig. 2. These campaigns encompassed the following scenarios: (1) a conventional pullout test featuring an encapsulation length of 1000 mm

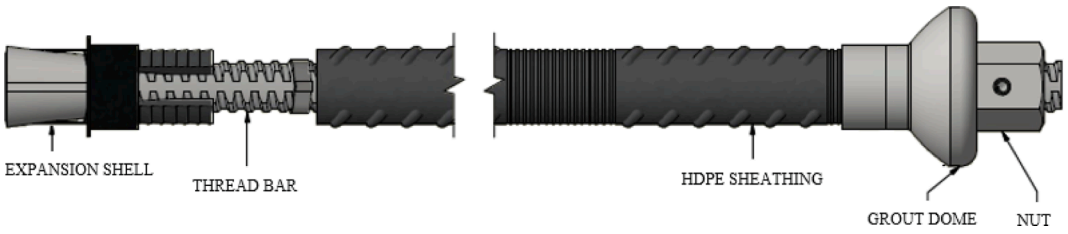

Fig. 1. HDPE protective sheathed bolt (DSI Australia, 2018).

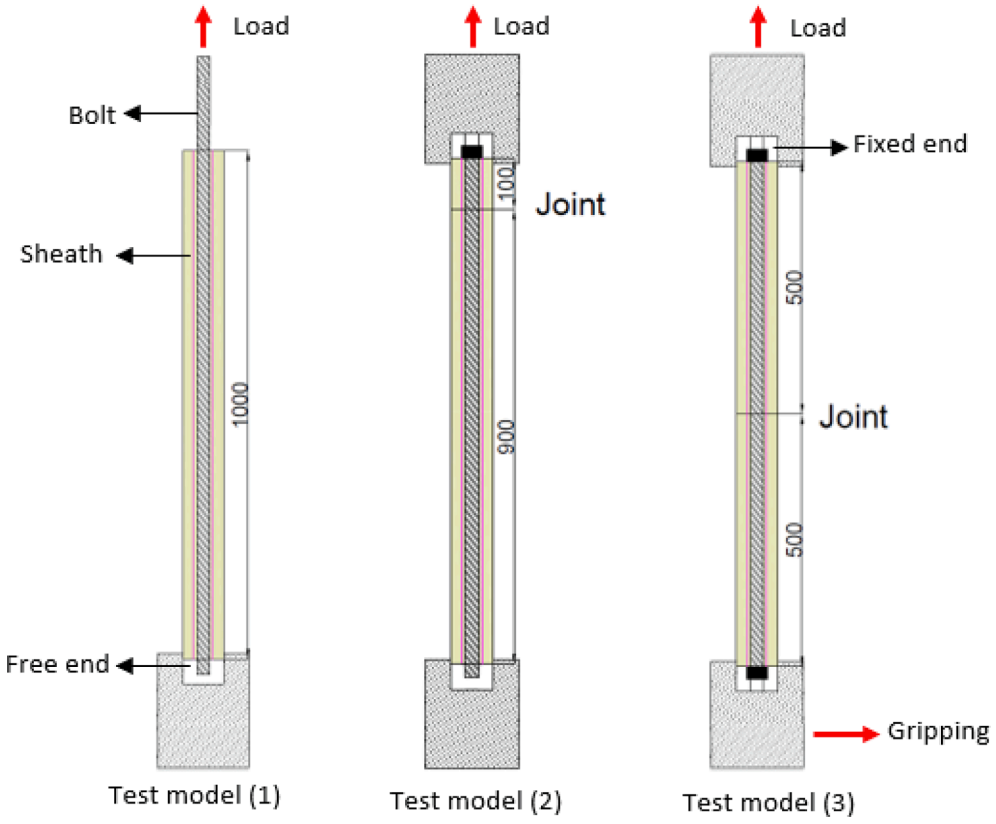

Fig. 2. Schematic view of the testing design.

and a free end, with the pullout load applied directly on the bolt; (2) a double embedment pullout test employing an encapsulation length of 900 mm, still with a free end, but the load being applied on the steel pipes and the other end is fixed; and (3) a double embedment pullout test featuring an effective encapsulation length of 500 mm, without any free end, and with the load applied to the steel pipe. The intent behind the first testing configuration was to replicate in situ pullout testing conditions, where the load acts directly on the bolt. In the second testing configuration, the purpose was to simulate practical field conditions where the potential failure of one component (either the external fixtures like the nut/dome or the expansion shell) could lead to bolt slip. It is important to note that the other side was securely welded, thereby preventing any slip. The third test was designed to simulate a scenario in the field where both the external fixtures and the expansion shells retain their structural integrity until the steel bar's ultimate capacity is reached. Hence, the primary objective was to assess the system's integrity, particularly focusing on the condition of the protective sheath as the load approached the tensile strength of the bars. For the latter two designs, a joint was incorporated to replicate the presence of a rock mass discontinuity, representing the point where the slip of rock blocks is initiated, thereby activating the bolts. Throughout the tests, the opening of the joint was tracked using a Linear Variable Differential Transformer (LVDT) to assess the condition of the plastic sheath against displacements. This monitoring assumes significance for designers and engineers, as the plastic sheath must remain intact and undamaged to provide enduring protection against corrosion for the system's entire lifespan.

The experimental design comprised two types of bolts, namely Type-1 and Type-2, which have a nominal diameter of 26 mm and 21 mm, respectively. The protective sheaths comprise a plastic pipe-shaped High Density Polyethylene (HDPE) featuring indentations on the inner surface and oval-shaped bulges on the outer surface. These sheaths possess internal diameters of 37.6 mm and 29.2 mm, manufactured for Type-1 and Type-2 bolts, respectively. The protective plastic sheaths exhibit two types of irregularities on their external surface: circumferential threads and embossed ridges. Additionally, the internal surface features dents. Fig. 3 provides an overview of the bolts and protective sheaths employed in the study, while Table 1 tabulates the geometric and mechanical attributes of these bolts. Additionally, Fig. 4 and Fig. 5 depict the tensile behavior of both the bolts and sheaths. The discrepancy in tensile strength between Type 1 and Type 2 bolts, shown in Fig. 4, is because of

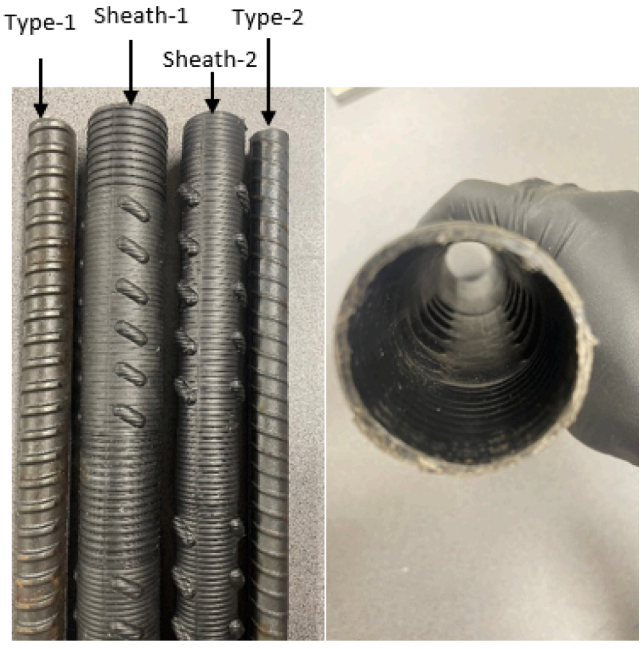

Fig. 3. Bolts and protective sheaths used in the study.

Table 1
Geometric and mechanical characteristics of the protective sheathed bolts used in the tests.

Bolt type	Nominal diameter	Sheath outside diameter	Sheath thickness	Bolt's elastic modulus	Bolt's Yield strength	Bolt's tensile strength	Bolt's A_{gt}	Sheath's elastic modulus	Sheath's tensile strength
	(mm)	(mm)	(mm)	(GPa)	(kN)	(kN)	(%)	(GPa)	(MPa)
Type-1	26	43.6	3	200	530	620	8	0.3	16
Type-2	21	35.2	3	200	220	360	8	0.3	16

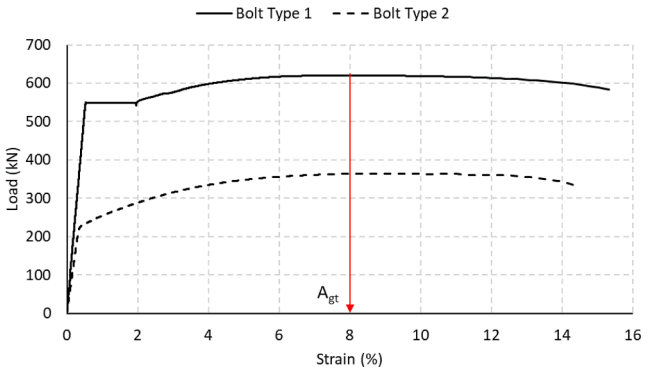

Fig. 4. Elongation behavior of the Type 1 and Type 2.

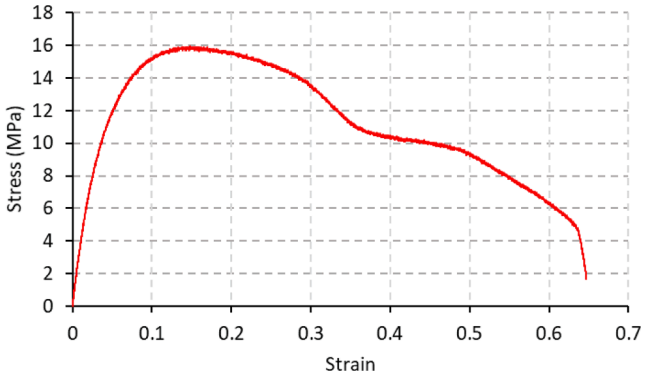

Fig. 5. Tensile behavior of the HDPE sheath used in the tests.

differences in their structural design, manufacturing methods, chemical compositions, and fabrication processes, leading to distinct mechanical properties. For instance, the Type-1 bolt has a diameter of 26 mm, with yielding and ultimate strengths of 530 kN and 620 kN, respectively. In contrast, the Type-2 bolt features a nominal diameter of 21 mm, with yielding and ultimate strengths of 220 kN and 360 kN, respectively.

In total, six distinct testing scenarios were designed, and specific scenarios were repeated to ensure the precision of the test results. This repetition aimed primarily at validating the grouting, material, and testing design to prevent any potential deficiencies or malfunctions, particularly in the test setup. A crucial consideration for this repetition was to guarantee the correct installation of strain gauges and prevent any damage during the grouting process, ensuring consistent and accurate recording of strain values. Table 2 provides a comprehensive overview of the testing plan.

1.2. Specimens design and preparation

A selection of materials was made to thoroughly evaluate the axial behavior of the protective sheathed bolts across various designs. These materials included bolts with the plastic protective sheaths, steel hollow bars as the surrounding materials (Fig. 6a), cementitious grout as the bonding agent. The steel hollow bars, having an 80 mm outer diameter and a 12 mm thickness, were internally rifled (Fig. 6b). This internal

Table 2
Summary of the testing campaign.

Test ID	Testing model*	Bolt type	Effective encapsulation length (mm)	Number of tests	Bolt slip
A	(1)	Type-2	1000	1	Bolt can slip at both free end and loading end
B	(2)	Type-2	900	2	Bolt can only slip at free end
C	(3)	Type-2	500	2	Slip is not allowed
D	(3)	Type-2	500	1	Slip is not allowed
E	(2)	Type-1	900	2	Bolt can only slip at free end
F	(3)	Type-1	500	2	Slip is not allowed

* Refer to Fig. 2.

rifling served two purposes: simulating field conditions and preventing failures at the junction of the hollow bar and the grout. Additional accessories were designed and manufactured to facilitate the centralization of the bolts and to enhance the grouting process.

A specialized approach was implemented to assess bolt deformation along the encapsulation length and to derive the axial load distribution and bond stress across this length. Specifically, the steel bars underwent design modifications for tests (2) and (3). These modifications involved incorporating double-sided triangular grooves, each covering an area of approximately 20 mm^2. The grooves were designed with the specific purpose of offering an optimal surface for the installation of resistive strain gauges. These gauges, with a length of 3 mm and a resistance of 120 O, were precisely mounted onto these grooves for accurate strain measurement. Figs. 7 and 8 illustrates both the arrangement of the grooves and the placement of the resistive strain gauges on the bolt.

In the process of encapsulating the bolts within the hollow bars, a cementitious grout was employed. This grout was prepared by mixing it with water at a grout ratio of 22 %, and it was subsequently pumped into the samples to ensure the complete filling of the gaps between the bar and the plastic sheath, and also between the plastic sheath and the hollow bar. The compressive strength of the grout was determined to be approximately 53 ± 1.2 MPa. Fig. 9 shows the prepared specimen for testing model (3). As previously noted, the specimen arrangement in the testing model (1) was devised to allow movement of the bar at both ends. However, in the case of the testing model (2), one end of the bolt was permitted to move freely, whilst the opposite end was welded in order to restrain its movement. Conversely, testing model (3) involved welding the bolts at both ends, immobilizing any potential movement along the bolt's length. Fig. 10 illustrates the ends of the specimens according to test objectives.

The samples were tested using a large-scale 1000 kN universal testing machine. The application of load was achieved through a hydraulic system, with calibrated load cells and LVDTs employed for measuring both the load and displacement. Upon placing the specimen in the testing machine, the clamps located on the upper crosshead and middle crosshead were tightened to secure the specimens using flanges that were screwed onto the specimens (Fig. 11). Additionally, apart from

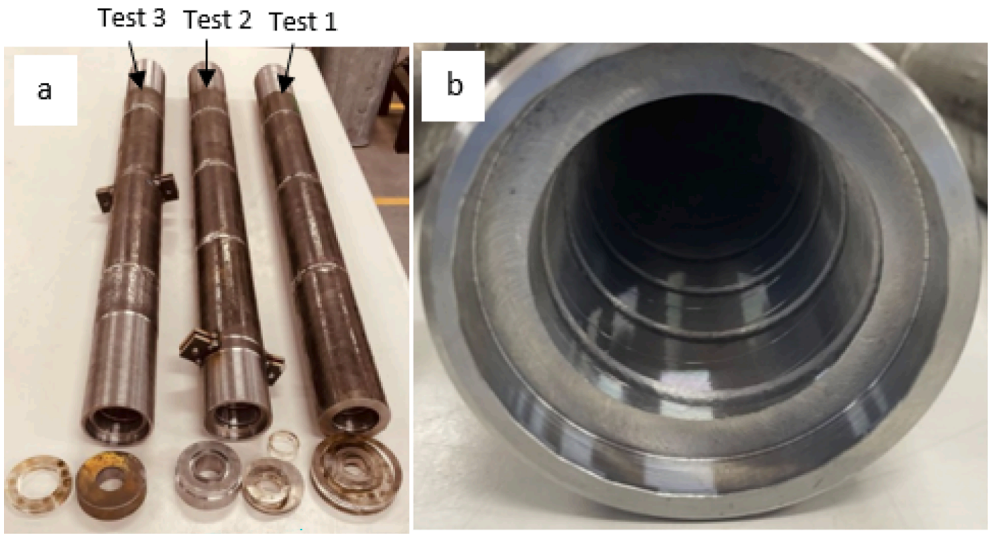

Fig. 6. The materials used for specimen preparation including a) the manufactured hollow bars as confinement, and b) the internal rifling of the hollow bars.

Fig. 7. Grooves, instrumentation, and mounting strain gauges on the steel bars.

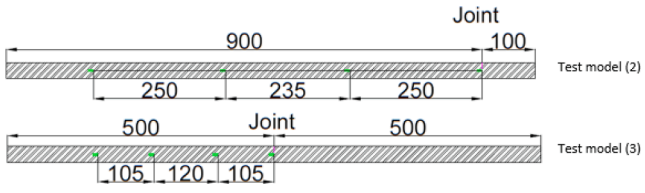

Fig. 8. Positions of the strain gauges installed on the bars.

the load sensors incorporated within the 1000 kN machine, one LVDT was installed on the simulated joint to measure the displacement of the joint, as depicted in Fig. 12.

2. Test results and discussion

The findings from the pull tests were analyzed and discussed from three distinct perspectives:

1) Load-Displacement relationship: this section explores the connection between applied load and displacement obtained from the pull tests.
2) Load distribution along the encapsulation length: the distribution of load along the length of the encapsulation is examined in this section.
3) Failure mechanism investigation: the failure mechanism is studied through the longitudinal slicing of the specimens and detailed observational analysis.

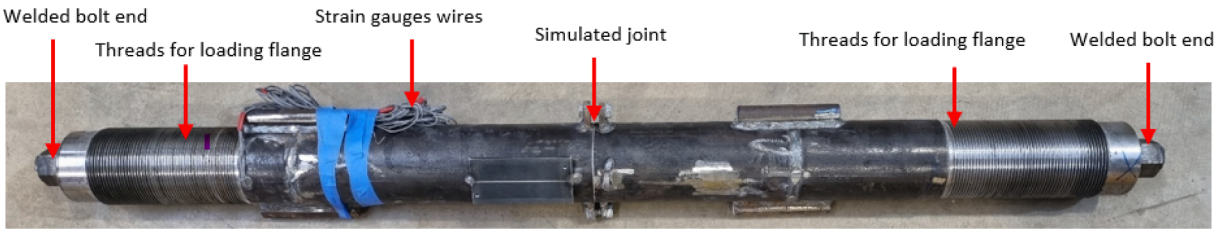

Fig. 9. Completed specimen for test model (3).

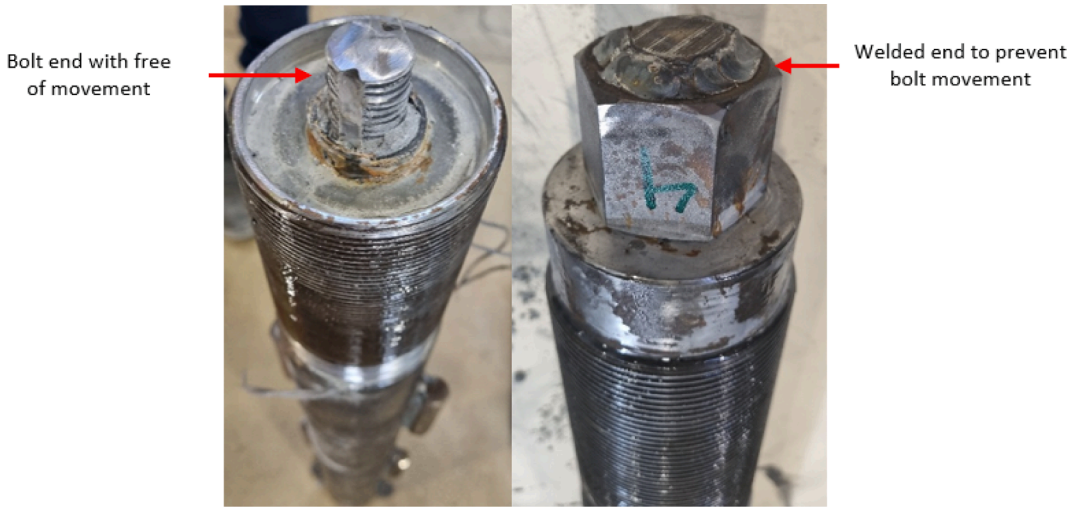

Fig. 10. Conditions of the bolt ends to fulfil the test objectives.

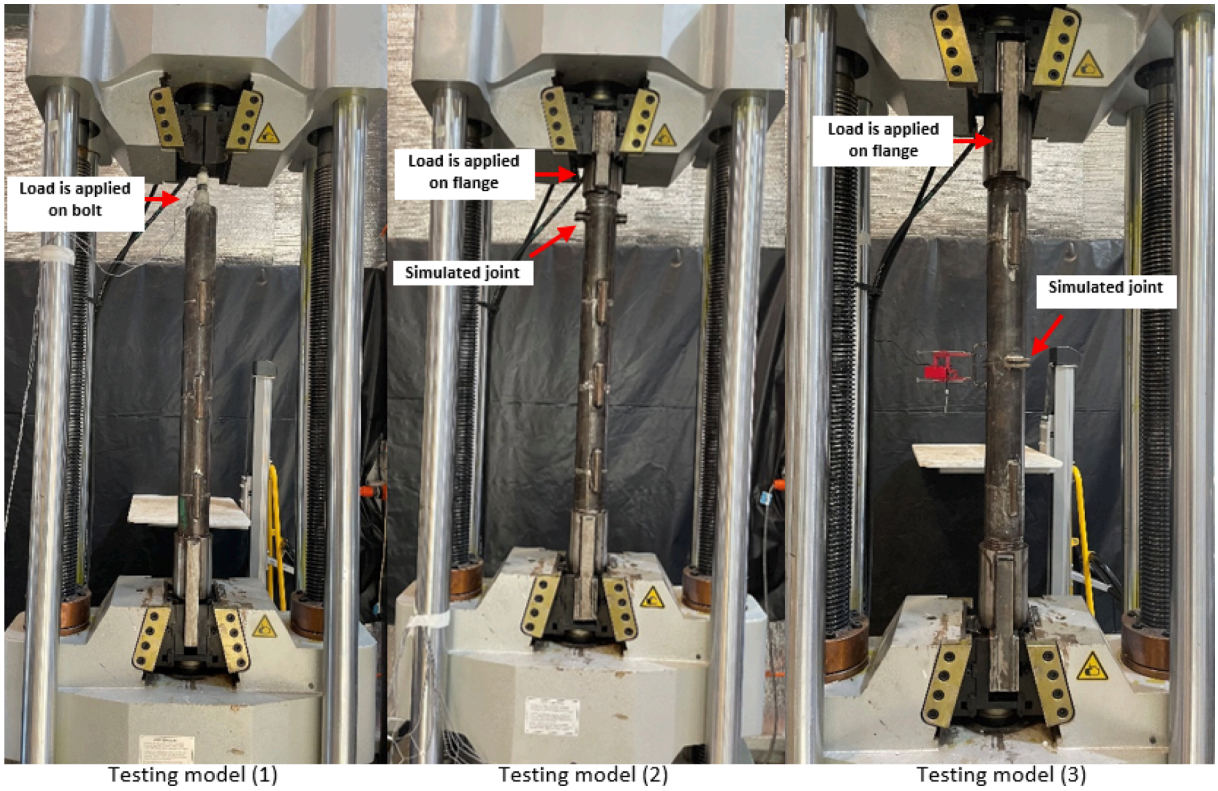

Fig. 11. Testing setup for different experimental programs.

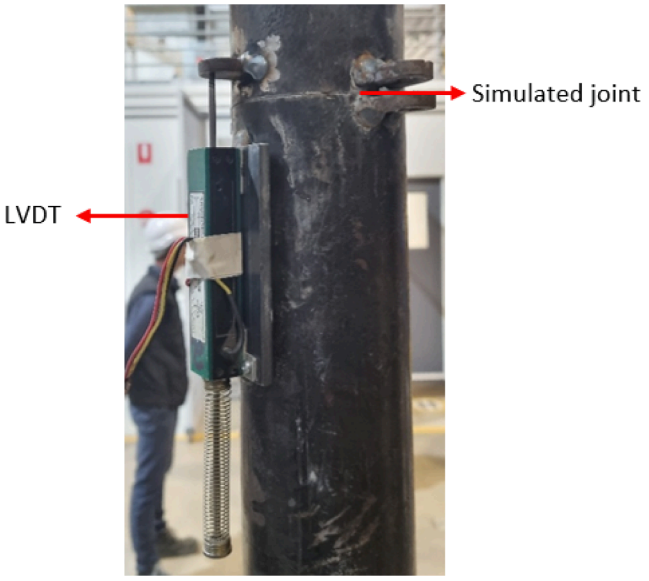

Fig. 12. LVDT installed on the joint to measure the corresponding displacements.

2.1. Load-displacement relation

Fig. 13 illustrates the load–displacement curves derived from pull tests conducted on the Type-1 bolts using different testing models. Among the specimens, Tests A and B exhibited failures due to debonding at the grout-sheath interface, while specimen D experienced failure due to bar rupture. In specimen C, the test was halted at 2.5 % elongation to investigate the protective sheath conditions at this specific elongation.

In both series A and B, regardless of the loading arrangement, similar load–displacement behavior was observed. As depicted in Fig. 13, in Series A, the load increased linearly with displacement up to 498 kN at 16.2 mm displacement. Beyond this point, the load remained nearly constant with further displacement. This point (498 kN, 16.2 mm) marked the onset of global debonding within the system. The initial linear growth indicated elongation of the steel bar, potentially causing damage to the grouting materials near the loading point. The relevant literature suggests that conventional fully grouted rock bolts exhibit shear-off damage at the bolt-grout interface in such cases (Cui et al., 2020; Hyett et al., 1992). However, these tests yielded circumferential cracks within the grout-filled space between the bolt and the sheath, deviating from shear-off damage. These circumferential cracks most likely stemmed from induced tensile stress within the grout due to the elongation of the bolt. Cracks were initiated once this tensile stress approached the grout's tensile strength. The bolt and grout column were

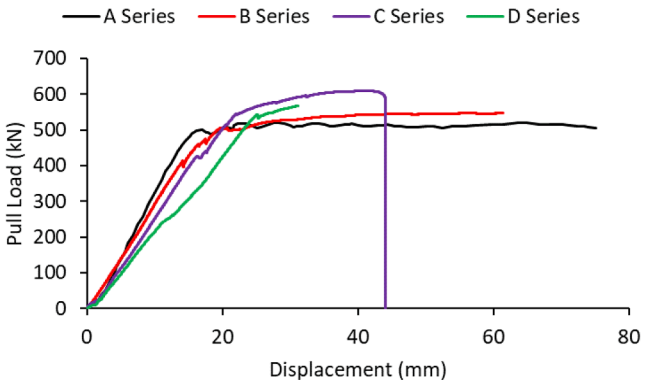

Fig. 13. Load-displacement relation for the tests conducted on the Type-2 bolts.

extracted from the system during specimen A's debonding process, as depicted in Fig. 14. For an in-depth analysis of the post-test failure patterns, refer to Section 4.3.

The load–displacement relationship in the series B test mirrors that of series A. Once the load reaches 502 kN at 19.9 mm displacement, the load increase relative to displacement drops, and further load increments occur only minimally. The variation in load and displacement values at which debonding of the systems initiates in series A and B can be ascribed to the plastic sheath's efficacy in series B, slightly shifting the corresponding point to the right. Fig. 15 shows specimen B following the test. As depicted, the protective plastic sheath underwent rupture caused by considerable stretching. Nevertheless, monitoring the specimen's conditions during the test revealed the plastic sheath remained intact until reaching a displacement of 27 mm. Additionally, there was an observable 47 mm slip at the free end, as illustrated in Fig. 15.

The results obtained from the testing of series A and B demonstrate that when the bolt is permitted to slip, the grout-sheath interface emerges as the most vulnerable element within the system (the encapsulation length is under 1000 mm), where debonding failure occurs. This failure at this interface can be attributed to inadequate friction between the grout and the inner surface of the sheath. This friction deficiency might be attributed to the specific configuration of the plastic sheath's inner surface.

In contrast, the load applied to specimen C surpassed the yield strength of the bar, which is approximately 535 kN. This caused the bolt to deform plastically and reach the ultimate tensile strength, measured at 610 kN. This was followed by necking and eventually, the bolt ruptured at a displacement of 44 mm. During testing, it was observed that the sheath stretched alongside the bolt's deformation. The sheath remained intact until the bolt ruptured, at which point the sheath was torn completely (Fig. 16). The results of test C highlight that the load levels in tests A and B remained below the bar's yield strength. This indicates that the critical embedment length in this specific bolting system exceeds 1000 mm.

Test D followed the same approach as test C, yielding comparable results. However, the test was concluded at around 31 mm displacement, equivalent to a load of 568 kN. This was done to specifically monitor the condition of the specimen, particularly the state of the protective sheath, at this specific displacement. Fig. 17 illustrates that the sheath remained undamaged and intact, indicating that the corrosion protection measure effectively functions at this level of load and displacement.

Fig. 18 displays the load–displacement curves from tests E and F. Despite differing specimen arrangements, the curves exhibit similar behavior. In test E, where the bar slip from the free end was allowed, the bolt's encapsulation length was adequate to surpass its yield strength (230 kN at 10 mm displacement). Progressing further, the system reached its ultimate tensile strength (320 kN at 45 mm displacement), ultimately rupturing at 285 kN and a displacement of 50 mm. The conditions of the specimen post-test are depicted in Fig. 19a. Monitoring during testing revealed that the plastic sheath's strength properties closely resembled those of the sheath utilized in Type-2 bolts. This similarity was evident as both sheaths sustained damage at a displacement of 28 mm.

2.2. Bond stress distribution along the encapsulation length

Bond pertains to the resistance to shear forces that develops between the bolt and the materials it is bonded to when subjected to a pullout load. Research has revealed that the stress distribution resulting from this bonding at the interface of the bolt and grout and along the length where the rock bolt is fully embedded is not consistent. Despite this, it is often assumed that bond stress distribution is uniform in cases involving short embedded specimens. The measurement of the extent of longitudinal elongation of the bolt along its embedded length through devices like strain gauges allows for the technical quantification of this bond

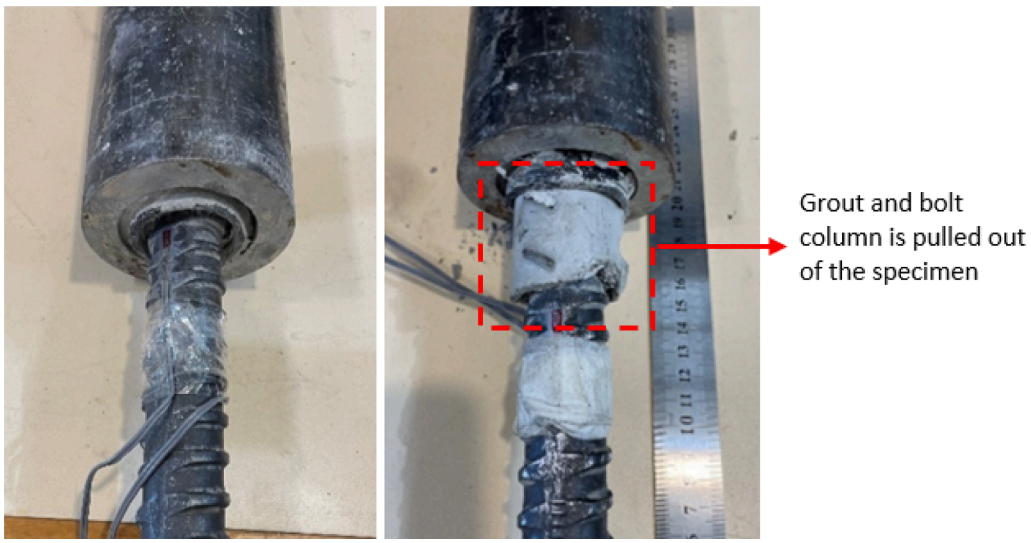

Fig. 14. Conditions of the specimen in the series A test: before test (left) and after test (right).

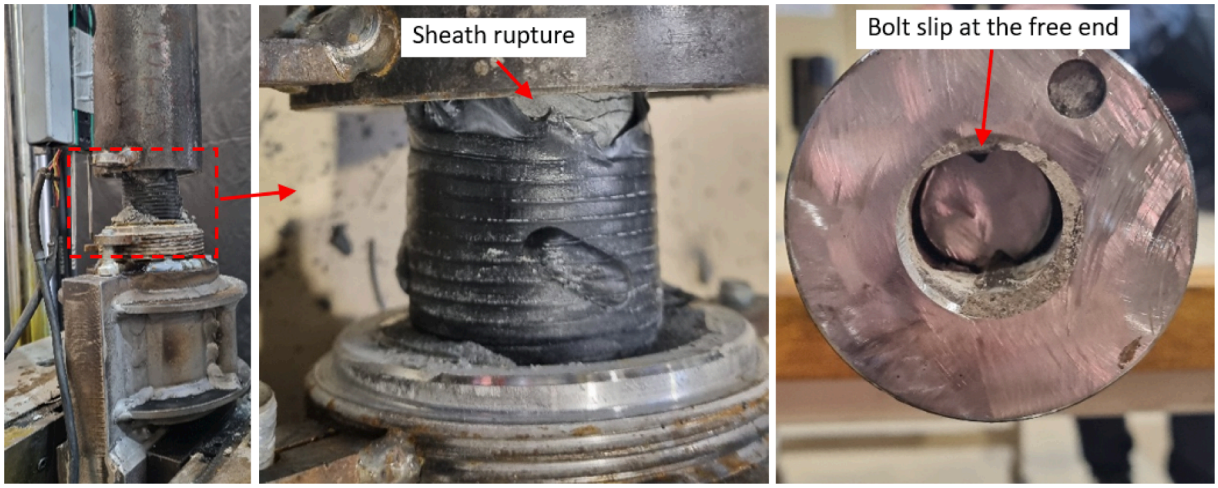

Fig. 15. Conditions of specimen B after testing.

stress distribution. In Fig. 20, a schematic is given of the stress equilibrium within a section of a grouted bolt with a specific length (Δx). Under the assumptions of four key conditions, namely 1) the problem is in the elastic stage, 2) a uniform distribution of bond stress across Δx; 3) the absence of energy dissipation in other forms like the creation of fractures, cracks, or damage; and 4) the absence of deformation in the surrounding rock; the force equilibrium equation for Fig. 20 can be formulated as follows:

$$f_b + \delta f_b = f_b + \overline{\tau}_{bu}(\pi d_b \Delta x) \tag{1}$$

where $f_b + \delta f_b$ is the force applied at strain gauge 1, while f_b signifies the force within the bolt at strain gauge 2. The interfacial shear stress at the bolt and grout interface is denoted as $\overline{\tau}_{bu}$, and d_b stands for the bolt's nominal diameter. The separation between the strain gauges is represented by Δx.

Applying constitutive equation ($\sigma = \varepsilon.E$) in Eq.1 the following equation is achieved:

$$(\varepsilon + \delta\varepsilon)Ea_b = \varepsilon E a_b + \overline{\tau}_{bu}(\pi d_b \Delta x) \tag{2}$$

where $\varepsilon + \Delta\varepsilon$ is the strain measured by strain gauge 1, E is the elastic modulus of the bolt, a_b is the cross area of the bolt and ε is the strain measured by strain gauge 2.

By simplifying Eq. (2), interfacial bond stress along Δx can be achieved as follows:

$$\overline{\tau}_{bu} = \frac{\delta\varepsilon E d_b}{4\Delta x} \tag{3}$$

Hence, monitoring the elongation of bolts throughout the embedded length due to the pullout force offers an efficient approach to ascertain the distribution of bond stress at the interface. This knowledge is crucial for the development of accurate models governing the axial behavior of rock bolts.

Fig. 21 shows that the distribution of bond stress generated along the grout interface in Tests B, C, E, and F. The measurements are taken at various distances from the loading point, with 50 kN load increment intervals. As shown, the pattern of bond stress distribution is influenced by both the specific test type and the system failure mode.

In the graphs depicted in Fig. 21, a consistent pattern is evident: at lower levels of axial loading, the interfacial bond stress is highest in the immediate vicinity of the load application point and progressively diminishes with increasing distance from it. It is important to highlight that based on the strain values observed during the pullout tests, the bond stress exhibited its peak in the immediate proximity of the joint at the commencement of the tests. However, as the load reached 35–43 kN

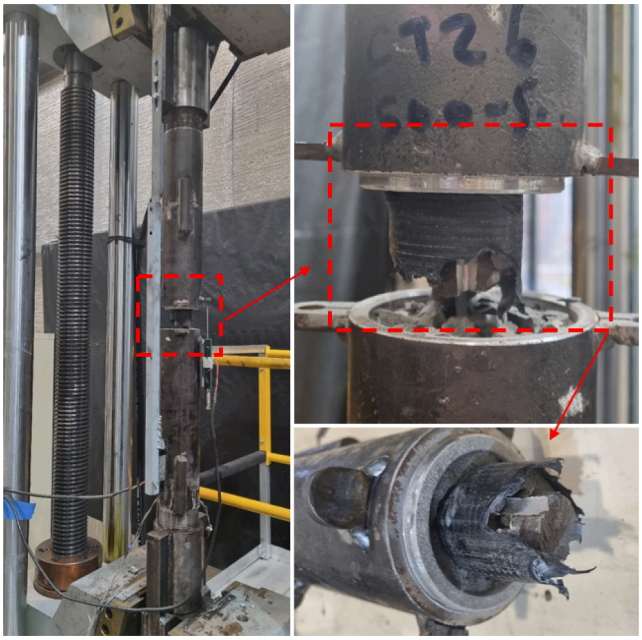

Fig. 16. The conditions of specimen C after testing.

Fig. 17. The conditions of specimen D after testing.

and 27–33 kN for Type-1 and Type-2 bolts, respectively, the bond stress sharply declined to zero. This decrease was attributed to the debonding of the grout at the joint. Consider Test B as an illustrative case, as presented in Fig. 21a. The interfacial bond stress between the first and second strain gauges, spanning a distance of 0–225 mm, achieves its maximum value of 7.5 MPa under a 350 kN axial load. However, the bond stress decreases the further one moves away from the load point.

When the applied axial load is less than 150 kN, the interfacial bond stress at a distance of 735 mm drops to zero. Conversely, when the load surpasses 150 kN, the bond stress remerges and gradually escalates with the increasing load. The reduction in bond stress beyond the 150 kN

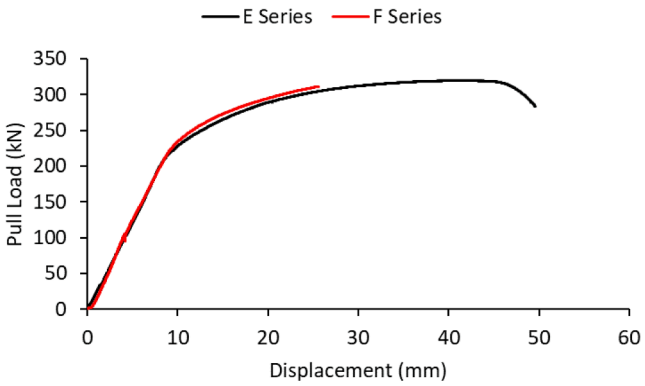

Fig. 18. Load-displacement relation for the tests conducted on the Type-1 bolts.

threshold at the 225 mm point can be attributed to the system's debonding, specifically in that region. By contrast with other cases, Fig. 21a demonstrates that once the applied load reaches 500 kN, the induced bond stress attains its peak, ranging between 7.7–8.7 MPa, within the distance interval of 485–735 mm. This particular behavior can be correlated with the observed failure mode in the specimen, characterized by debonding occurring at the grout-sheath interface, and a relatively constant load is sustained until the conclusion of the test. In instances where debonding occurs within a specimen section, such as the 0–225 mm range in Test B, the bond stress tends to shift deeper into the specimen and persists until complete debonding of the system is attained. Such behavior is conventionally observed in the context of fully grouted rock bolts. However, in the case of protective sheathed rock bolts, this behavior deviates, as failure predominantly manifests in two distinct modes: a rupture in the bolt shank and failure at the grout-sheath interface.

In Test C, as illustrated in Fig. 21b, a similar trend appears, with bond stress initially peaking in the proximity of the loading point and gradually diminishing with increasing distance. The bond stress was recorded at zero at a distance of 330 mm when subjected to a load of 150 kN or less. Analyzing the graph reveals that debonding within the 0–105 mm section occurs as soon as the applied load reaches 300 kN. Subsequently, the bond stress decreases within this section, while concurrently, bond stress increases in the deeper section, specifically the range of 105–225 mm. When the load reaches 500 kN, the bond stress significantly diminishes, nearly reaching zero at the 0–105 mm, 1.8 MPa at 105–225 mm and 1.7 MPa at 225–330 mm. This suggests that complete debonding occurred in the 0–225 mm section, and partial debonding at 225–330 mm. Consequently, once debonding occurs in a specific section, the bond stress redistributes to the adjacent section deeper within the encapsulation length.

In Test E, depicted in Fig. 21c, the highest recorded bond stress reached 6.4 MPa within the 0–225 mm range, corresponding to a 200 kN load. Partial debonding occurs in this section once the applied load exceeds 200 kN. Following a pattern observed in previous tests, debonding at 0–250 mm leads to a redistribution of bond stress to the 250–485 mm section, where the bond stress increases to 3.8 MPa at a 250 kN load. Reduction in the bond stress at the 250–485 mm section once the axial load increases to 300 kN can be associated with the debonding of the system at this section. The results indicate that full debonding is evident in the 0–250 mm segment, while in the 250–485 mm section, partial debonding resulted in a considerable reduction in bond stress.

In Test F, as illustrated in Fig. 21d, the bond stress initially increases with the applied load within the 0–105 mm range, reaching 5.2 MPa at 100 kN. Subsequently, a decrease in bond stress is observed due to partial debonding, ultimately leading to complete debonding within this section and the bond stress dropping to zero. There is a substantial

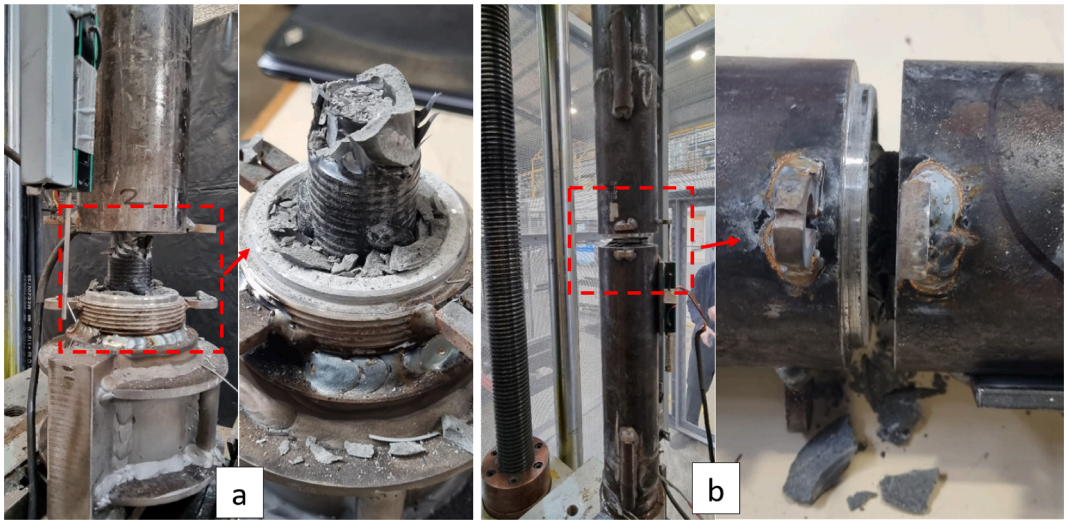

Fig. 19. Conditions of the Type-1 specimens after testing: a) test E and b) test F.

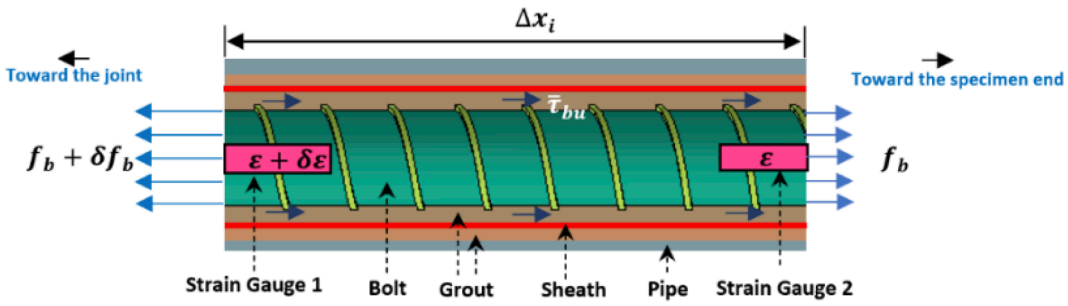

Fig. 20. Stress equilibrium in a length of embedded rock bolt.

increase in bond stress observed in the 105–225 mm section as soon as debonding occurs at 0–105 mm. The bond stress within the 105–225 mm section reaches 6.3 MPa, corresponding to a 200 kN load. However, the bond stress in this section decreases afterwards, indicating significant debonding in this region, with the bond stress transferring to the 225–330 mm section. The highest recorded bond stress within the 225–330 mm section reached 4.6 MPa, corresponding to a 300 kN pull load.

3. Failure mechanism of the specimens

Investigations into the failure modes of the specimens subjected to pullout conditions typically consider two key aspects: firstly, the rupture of the bolt that occurs at the joints, and secondly, failure that happen at the interface between the grout and sheath interface. It was observed that bolt rupture occurs when the encapsulation length is sufficiently long or when the anchoring and external fixtures are robust enough to withstand the applied load without failing. In this study, using a waterjet system to slice the specimens assisted to investigate the failure modes in sheath-protected bolts and to compare with the conventional rock bolting systems (Fig. 22).

Tests A and B share almost identical failure characteristics as shown in Fig. 22. In both cases, inclined cracks at the vicinity of the loading end and the joint and also circumferential cracks, oriented at approximately 90 degrees, are visible within the grout situated between the bolt and the protective sheath, spanning a length of about 130 mm. Beyond this point, no cracks were visible. Further investigations suggested that the circumferential cracks were likely resulted from tensile stress induced at the by the bolt's elongation and occurred once it exceeded the tensile strength of the grout. Consequently, the primary failure mode in Tests A and B can be attributed to slipping at the grout-sheath interface.

Fig. 23 schematically illustrates the failure mode observed in Tests A and B. As depicted, when the pullout load escalates to the F_1 level, debonding occurs at the bolt-grout interface, generating an inclined crack at this section. Subsequently, with a further increase in the pullout load to F_2, debonding occurs at the grout-sheath interface. Later failure is mainly due to the lack of sufficient interlocking and adhesion at the grout-sheath contact. Additionally, under Load F_2, the extensive elongation of the bolt induces higher tensile stresses in the grout column that may surpass the tensile strength of the grout and resulting in the formation of circumferential cracks.

In Test C (shown in Fig. 22), extensive cracking was evident over a distance of 210 mm from the joint, followed by inclined cracks with lower density extending another 290 mm. However, beyond this length, the grout appeared to be intact. This failure pattern closely aligned with the bond stress distribution presented in Fig. 21b. For instance, the reduction in bond stress at the 500 kN load within the 0–225 mm range indicated extensive debonding and failure in this segment. Consequently, the axial load was transferred toward the end of the specimen and resulted in reduced bond stress. It's also worth noting that the protective sheath experienced extensive stretching at the joint, leading to sheath rupture.

In Test E, grout damage was observed on the grout along the entire encapsulation length (Fig. 22). Due to slippage occurring at the grout-sheath interface, the irregularities formed on the grout were sheared off. Three types of cracks were identified along the encapsulation length: densely distributed cracks perpendicular to the bolt axis within the region located 200 mm from the joint, less densely distributed cracks perpendicular to the bolt axis from 200 mm to 400 mm, and a region from 400 mm to 900 mm where the grout appeared to be crushed. In the

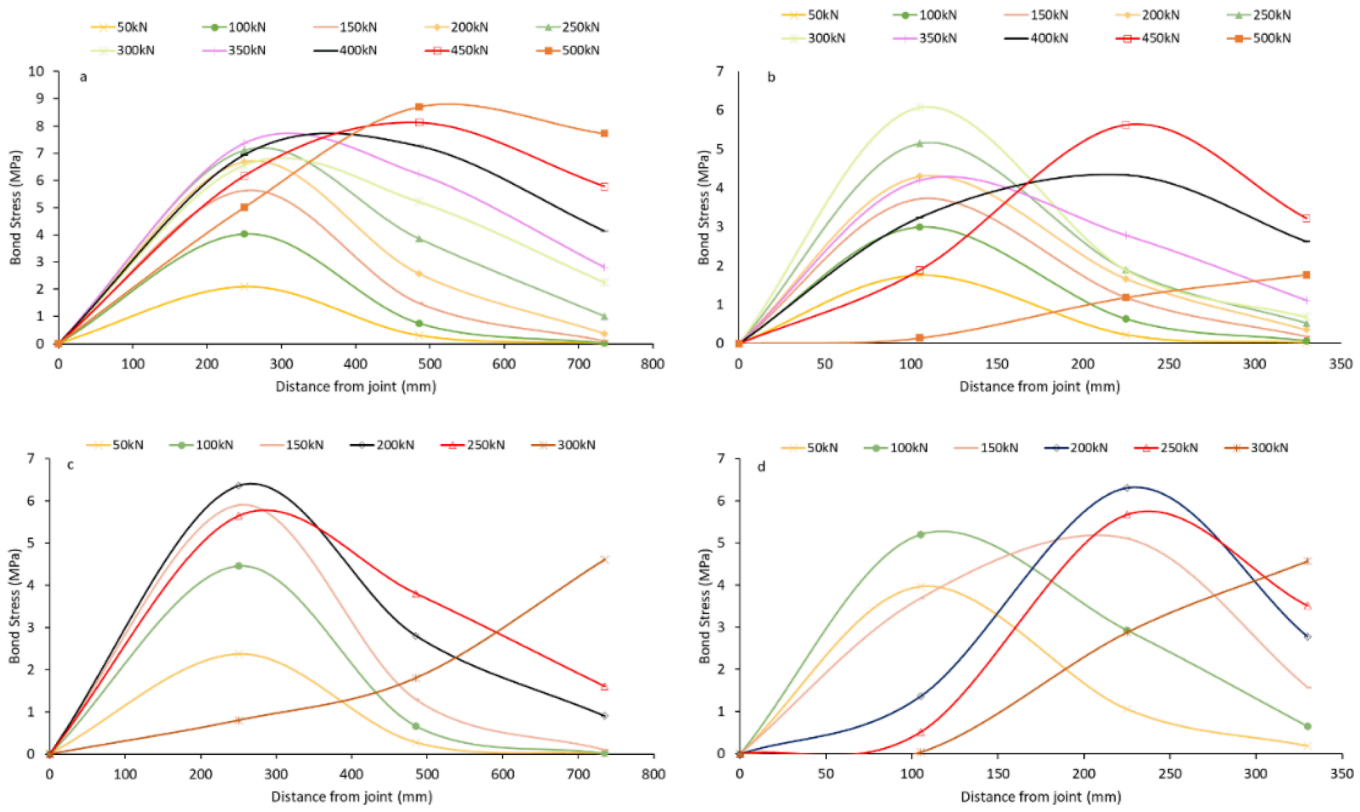

Fig. 21. Bond stress distribution along the encapsulation length for a) Test B, b) Test C, c) Test E and d) Test F.

first two regions, debonding was evident at the bolt-grout and grout-sheath interfaces. By contrast, in the third region, the grout at the bolt-grout interface seemed to remain intact without visible damage. This failure mode is closely aligned with the bond stress distribution presented in Fig. 21c as the low bond stress in the 0–485 mm section correlated with the described level of debonding. It can be concluded that while the grout was fully damaged at the grout-sheath interface (0–900 mm) and partially damaged at the bolt-grout interface (approximately 0–400 mm), the bolt failure occurred at the shank near the joint when the load reached 320 kN.

In Tests F (shown in Fig. 22), grout damage was observed at the bolt-grout interface on both sides of the joint (500–500 mm). The extent of grout damage, in terms of cracks between the bolt and sheath, extended to approximately 320 mm from the joint on both sides. Significant cracks were evident in the vicinity of the joint (within 120 mm). Importantly, there was no bolt slippage, as indicated by the intact irregularities on the grout surface created by the bolt ribs. This indicates that the grout's failure type was not shear-off but rather resulted from the induced elongation of the bolt. The circumferential cracks observed were a consequence of tensile stress rather than shear stress distribution at the bolt-grout interface.

4. Conclusion

In this study, the behavior of plastic-sheathed rock bolts under various testing conditions was investigated. The primary objective was to gain insights into how the inclusion of protective sheaths affects the transfer of axial loads in these bolts. Two types of protective sheathed bolts, Type-1 and Type-2 were examined, and three different test setups were designed to explore the behavior of rock bolting in a comprehensive way. To analyze bond stress distribution along the sheath, strain gauges were installed on the bolts, and six pull tests were conducted.

Overall, two distinct trends in the load–displacement curves were observed, regardless of the bolt type, depending on the test setup. When the expansion shell and external fixtures could sustain the tensile capacity of the bolt or when the encapsulation length exceeded a critical threshold (900 mm for Type-1 and over 1000 mm for Type-2), the system failed due to bolt rupture. In such cases, the load–displacement curves followed the tensile behavior of the bolts. If these conditions were not met, the system failed through debonding at the grout-sheath interface, known as slip failure.

Type-1 and Type-2 bolts experienced the first type of failure at peak loads of 320 kN and 610 kN, respectively. The second type of failure, characterized by grout-sheath interface debonding, was only observed in Type-2 bolts, commencing at a load of 500 kN, ultimately resulting in the extraction of the grout and bolt column from the specimen.

The analysis of strain gauge data revealed that bond stress distribution is dependent upon the specimen's failure mode. The peak bond stress measured within all specimens fell in the range of 6–8.7 MPa. It was observed that when debonding occurred in one section of the specimen, the bond stress in that section decreased and shifted to other sections. In slip failure cases, the bond stress remained relatively constant along the intact encapsulation length (7.7–8.7 MPa in Test B). However, in Test C, extensive debonding at a 500 kN load significantly reduced bond stress in those sections.

Complete debonding at the bolt-grout interface was not identified in any of the tests, which is a phenomenon frequently observed in traditional rock bolting systems when the encapsulation length is short. Instead, full debonding was observed at the grout-sheath interface in Tests A and B, indicative of slip failure. Generally, circumferential cracks oriented approximately 90° to the bolt's direction were also observed. These cracks resulted from the extensive elongation of the bolt, and the low adhesive and interlock strength between the grout and sheath allowed the induced tensile stress to surpass the grout's tensile strength, initiating crack formation. These failure patterns were effectively related to the distribution of bond stress.

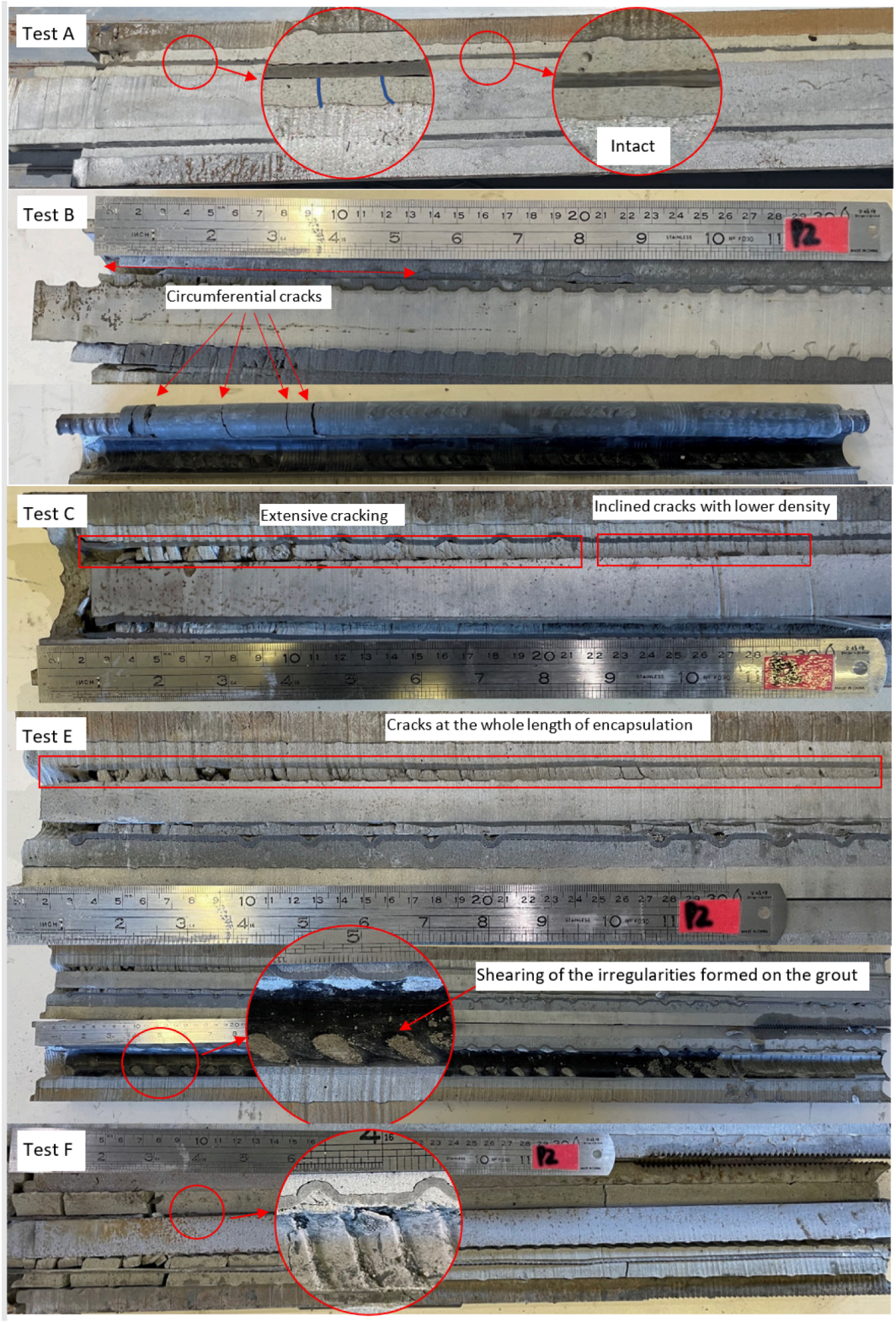

Fig. 22. Conditions of the specimens after testing.

5. Limitation of the study

The outcomes of this study reveal distinct axial behaviors and failure modes for protective sheathed rock bolts when compared to conventional rock bolts. Nevertheless, it is crucial to acknowledge and explore certain practical limitations. Given that these rock bolts are designed for installation in corrosive environments, we recognize the need for further investigation, particularly through a corrosion test applied to the overall system. This recommendation aims to address potential limitations and enhance the applicability of the study's findings in real-world scenarios.

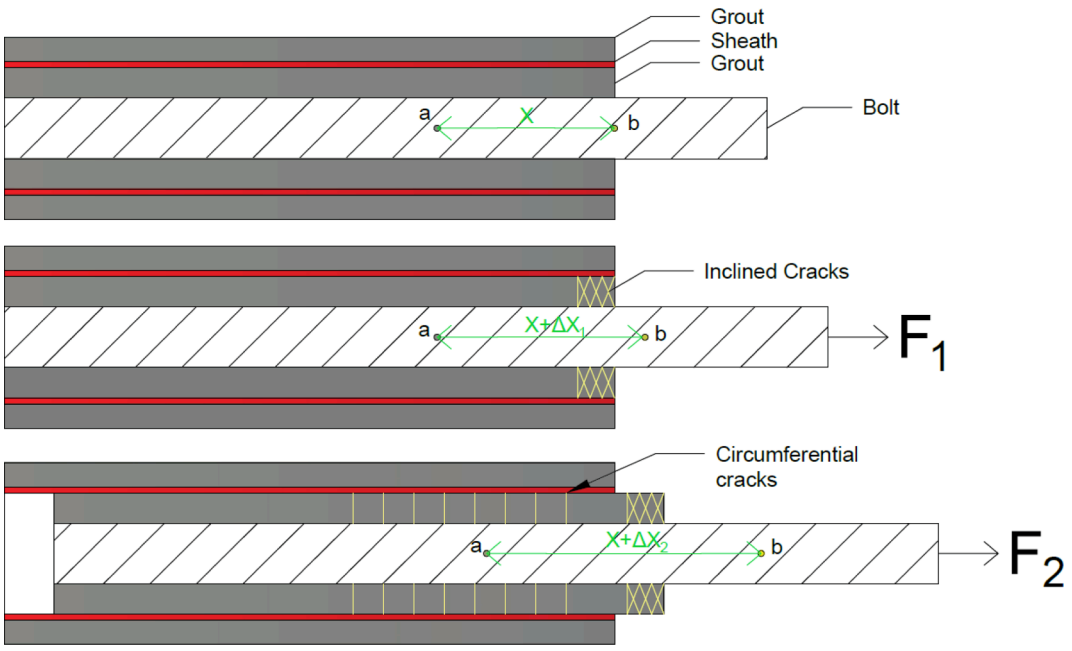

Fig. 23. Schematic illustrating the formation of inclined cracks and circumferential crack observed in Tests A and B.

CRediT authorship contribution statement

Hadi Nourizadeh: Conceptualization, Data curation, Formal analysis, Investigation, Methodology, Project administration, Software, Validation, Visualization, Writing – original draft, Writing – review & editing. **Ali Mirzaghorbanali:** Conceptualization, Formal analysis, Methodology, Writing – review & editing, Resources, Visualization. **Kevin McDougall:** Methodology, Supervision, Writing – review & editing. **Naj Aziz:** Methodology, Writing – review & editing.

Declaration of competing interest

The authors declare that they have no known competing financial interests or personal relationships that could have appeared to influence the work reported in this paper.

Data availability

Data will be made available on request.

References

DSI Australia, 2018. DSI Product Catalogue.
Aziz, N., Craig, P., Nemcik, J., Hai, F., Craig, P., Nemcik, J., Rock, F.H., Aziz, N., Craig, P., Nemcik, J., Hai, F., 2014. Rock bolt corrosion – an experimental study. Min. Technol. 9009. https://doi.org/10.1179/1743286314Y.0000000060.
Aziz, N., Mirzaghorbanali, A., Holden, M., 2017. The extent of shearing and the integrity of protective sleeve coating of cable bolts of protective sleeve coating of cable bolts. In: Coal Operators' Conference. Wollongong, Australia, pp. 240–246.
Bertuzzi, R., 2004. 100-year design life of rock bolts and shotcrete. Ground Support in Mining and Underground Construction. Taylor & Francis Group, London.
Cao, C., Jan, N., Ren, T., Naj, A., 2013. A study of rock bolting failure modes. Int. J. Min. Sci. Technol. 23, 79–88. https://doi.org/10.1016/j.ijmst.2013.01.012.
Chen, H., Kimyon, O., Ramandi, H.L., Manefield, M., Kaksonen, A.H., Morris, C., Crosky, A., Saydam, S., 2021. Microbiologically influenced corrosion of cable bolts in underground coal mines : The effect of Acidithiobacillus ferrooxidans. Int. J. Min. Sci. Technol. 31, 357–363. https://doi.org/10.1016/j.ijmst.2021.01.006.
Chen, H., Lamei, H., Craig, P., Crosky, A., Saydam, S., 2022. Stress corrosion cracking of cable bolts in tunnels : An in-situ testing approach. Tunn. Undergr. Sp. Technol. 123, 104421. https://doi.org/10.1016/j.tust.2022.104421.
Craig, P., Lamei, H., Chen, H., Vandermaat, D., Crosky, A., Hagan, P., Hebblewhite, B., Saydam, S., 2021. Stress corrosion cracking of rockbolts: An in-situ testing approach. Constr. Build. Mater. 269, 121275. https://doi.org/10.1016/j.conbuildmat.2020.121275.
Cui, G., Zhang, C., Pan, Y., Deng, L., Zhou, H., 2020. Laboratory investigation into effect of bolt profiles on shear behaviors of bolt-grout interface under constant normal stiffness (CNS) conditions. J. Rock Mech. Geotech. Eng. 12, 1234–1248. https://doi.org/10.1016/j.jrmge.2020.03.010.
Fahimifar, A., Ranjbarnia, M., 2009. Analytical approach for the design of active grouted rockbolts in tunnel stability based on convergence-confinement method. Tunn. Undergr. Sp. Technol. 24, 363–375. https://doi.org/10.1016/j.tust.2008.10.005.
Grasselli, G., 2005. 3D Behaviour of bolted rock joints: experimental and numerical study. Int. J. Rock Mech. Min. Sci. 42, 13–24. https://doi.org/10.1016/j.ijrmms.2004.06.003.
He, L., An, X., Zhao, Z., 2015. Fully grouted rock bolts: an analytical investigation. Rock Mech. Rock Eng. 1181–1196. https://doi.org/10.1007/s00603-014-0610-0.
Hyett, A.J., Bawden, W.F., Reichert, R.D., 1992. The effect of rock mass confinement on the bond strength of fully grouted cable bolts. Int. Rock Mech. Min. Sci. Geomech. Abstr. 29, 503–524.
Kilic, A., Yasar, E., Atis, C.D., 2003. Effect of bar shape on the pull-out capacity of fully-grouted rockbolts. Tunn. Undergr. Sp. Technol. 18, 1–6. https://doi.org/10.1016/S0886-7798(02)00077-9.
Li, C.C., 2017. Principles of rockbolting design. J. Rock Mech. Geotech. Eng. 9, 396–414. https://doi.org/10.1016/j.jrmge.2017.04.002.
Li, C.C., Stjern, G., Myrvang, A., 2014. A review on the performance of conventional and energy-absorbing rockbolts. J. Rock Mech. Geotech. Eng. 6, 315–327. https://doi.org/10.1016/j.jrmge.2013.12.008.
Ma, S., Nemcik, J., Aziz, N., 2013. An analytical model of fully grouted rock bolts subjected to tensile load. Constr. Build. Mater. 49, 519–526. https://doi.org/10.1016/j.conbuildmat.2013.08.084.
Ma, K.J., Stankus, J., Faulkner, D., 2018. Development and evaluation of corrosion resistant coating for expandable rock bolt against highly corrosive ground conditions. Int. J. Min. Sci. Technol. 28, 145–151. https://doi.org/10.1016/j.ijmst.2017.12.023.
Martín, L.B., Tijani, M., Hadj-hassen, F., 2011. A new analytical solution to the mechanical behaviour of fully grouted rockbolts subjected to pull-out tests. Constr. Build. Mater. 25, 749–755. https://doi.org/10.1016/j.conbuildmat.2010.07.011.
Nourizadeh, H., Mirzaghorbanali, A., Mcdougall, K., Jeewantha, L.H.J., Craig, P., Motallebiyan, A., Jodeiri, B., Rastegarmanesh, A., Aziz, N., 2023a. Characterization of mechanical and bonding properties of anchoring resins under elevated temperature. Int. J. Rock Mech. Min. Sci. 170, 105506. https://doi.org/10.1016/j.ijrmms.2023.105506.
Nourizadeh, H., Mirzaghorbanali, A., Serati, M., Mahmoud, M.-A., McDougall, K., Aziz, N., 2023b. Failure characterization of fully grouted rock bolts under triaxial testing. J. Rock Mech. Geotech. Eng. https://doi.org/10.1016/j.jrmge.2023.08.013.
Peter, K., Moshood, O., Oluwatomisin, P., 2022. An overview of the use of rockbolts as support tools in mining operations. Geotech. Geol. Eng. 40, 1637–1661. https://doi.org/10.1007/s10706-021-02005-5.
Rastegarmanesh, A., Mirzaghorbanali, A., McDougall, K., Aziz, N., Anzanpour, S., Nourizadeh, H., Moosavi, M., 2022. Axial performance of cementitious grouted cable bolts under rotation constraint scenarios. Rock Mech. Rock Eng. https://doi.org/10.1007/s00603-022-02950-4.
Singh, P., Spearing, A.J.S., Jessu, K., 2020. Analysis of the combined load behaviour of rock bolt installed across discontinuity and its modelling using. Geotech. Geol. Eng. 38, 5867–5883. https://doi.org/10.1007/s10706-020-01398-z.

Singh, P., Jang, H., Spearing, A.J.S., 2022. Improving the numerical modelling of in-situ rock bolts using axial and bending strain data from instrumented bolts. Geotech. Geol. Eng. 40, 2631–2655. https://doi.org/10.1007/s10706-022-02051-7.

Thompson, A.G., Villaescusa, E., Windsor, C.R., 2012. Ground support terminology and classification: an update. Geotech. Geol. Eng. 30, 553–580. https://doi.org/10.1007/s10706-012-9495-4.

Villaescusa, E., Wright, J., 1999. Reinforcement of underground excavations using the CT Bolt. In: Rock Support and Reinforcement Practice in Mining. Routledge, London. https://doi.org/10.1201/9780203740460.

Windsor, C.R., 1997. Rock reinforcement systems. Int. J. Rock Mech. Min. Sci. 34, 919–951.

Wu, S., Lamei, H., Chen, H., Crosky, A., Hagan, P., Saydam, S., 2019. Mineralogically influenced stress corrosion cracking of rockbolts and cable bolts in underground mines. Int. J. Rock Mech. Min. Sci. 119, 109–116. https://doi.org/10.1016/j.ijrmms.2019.04.011.